Journal of Physics and Chemistry of Solids 194 (2024) 112222

Contents lists available at ScienceDirect

Journal of Physics and Chemistry of Solids

journal homepage: www.elsevier.com/locate/jpcs

Ab initio Investigation of quasi-one-dimensional ternary chalcogenides Sr_2ZnX_3 (X = S, Se, Te) for efficient photovoltaic and thermoelectric applications

Chethan V., Mahendra M. *

Department of Studies in Physics, University of Mysore, Manasagangotri, Mysuru 570 006, Karnataka, India

ARTICLE INFO

Keywords:
Transition metal chalcogenides
Structural and electronic properties
Spin–orbit coupling
Thermo-electric figure of merit (ZT)
Density functional theory (DFT)

ABSTRACT

The quest for sustainable and renewable energy sources has become a vital global mission. Transition metal chalcogenide materials have garnered significant attention due to their unique low-dimensional physical properties. In this work, we explore the impact of ionic radius in modulating the physical properties of ternary chalcogenides by calculating structural, electronic, optical, and thermoelectric properties of Sr_2ZnX_3 (X = S, Se, Te) materials using first-principles density functional theory (DFT) as implemented in the WIEN2k program. To evaluate the effect of ionic radius, two novel semiconductors Sr_2ZnSe_3 and Sr_2ZnTe_3, were constructed using similar isostructural material Sr_2ZnS_3. Further optimized structure reveals that the corner-sharing ZnX_4 tetrahedra extended along the *b*-axis confirms the quasi-one-dimensional (Q1D) nature of Sr_2ZnX_3 materials. Band structure analysis revealed a wide direct bandgap nature with the values of Sr_2ZnS_3 (3.4 eV), Sr_2ZnSe_3 (2.8 eV) and Sr_2ZnTe_3 (1.75 eV), respectively. The lower effective mass of electrons and holes suggests higher carrier mobility and charge recombination rates, vital for photovoltaic applications. The optical properties of the materials are studied in the energy range of 0–10 eV (IR–Vis–UV region). We found that Sr_2ZnTe_3 material exhibits higher values of dielectric function, absorption coefficient ($\alpha \approx 10^6$ cm^{-1}), refractive index, and lower reflectivity, which indicates its suitability for photovoltaic application. Thermoelectric properties are crucial for assessing material utility in thermoelectric applications, and the study revealed substantial values of the Seebeck coefficient, electrical conductivity, figure of merit (ZT) greater than 2, power factor, and lower electronic thermal conductivity. The studied properties signify Sr_2ZnX_3 materials as potential candidates for light-emitting semiconductors and thermoelectric applications.

1. Introduction

Sr_2ZnS_3, Sr_2ZnSe_3, and Sr_2ZnTe_3 belong to the general group of quasi-one-dimensional transition metal chalcogenides with the general formula A_2MX_3 (A = Ba, Sr; M = Co, Fe, Mn, Zn; X = S, Se, Te) [1], which has recently gained significant interest owing to their applications in optical communication, laser advancements, narrow wavelength optical devices [2], solar cells [3], as well as in light-emitting diodes [4], thermoelectric materials and detectors for gamma and X-rays at room temperature [5,6] etc. Chalcogenides of divalent first-row transition metals (M = Mn, Fe, Co, Zn) display insulating properties with short-range antiferromagnetic ordering along chains. It is noted that this family of structures consists of linear chains of corner-sharing MX_4 tetrahedra, with two different A atoms positioned in between the chains [7]. Mehdi D. Esrafili et al. used *ab initio* calculations to examine the geometry minimization, interaction energies, and bonding properties of chalcogen (Y = S, Se) and halogen (X = F, Cl, Br) bond interactions. Their study revealed that chalcogen bonds are favored over halogen bonds for all the studied binary YOX_4:NH_3 complexes [8,9].

Sr_2ZnS_3 material is isostructural with K_2AgI_3, which crystallizes in the orthorhombic space group D_{2h}^{16}−Pnma. V. Petrykin et al. successfully synthesized Sr_2ZnS_3 a single-phase compound for the first time, and determined its crystal structure through single crystal X-ray diffraction data analysis. Additionally, their findings revealed that the phosphor Sr_2ZnS_3:Eu activated with Eu(II), exhibited bright golden-yellow light and which could be elicited by near-UV and blue light across a broad spectrum of excitation wavelengths [10].

Recently, the light-emitting diode properties of the Ba_2ZnS_3 material, which is isostructural to Sr_2ZnS_3, have been studied [11]. Subsequent investigations [12,13] revealed intriguing luminescent properties in the material. Notably, Ba_2ZnS_3 doped with Mn/Ce/Eu emerged

* Corresponding author.
E-mail address: mahendra@physics.uni-mysore.ac.in (Mahendra M.).

https://doi.org/10.1016/j.jpcs.2024.112222
Received 23 May 2024; Received in revised form 11 July 2024; Accepted 24 July 2024
Available online 29 July 2024

as a versatile phosphor, offering a spectrum of colors and finding applications in the development of white LEDs [14,15]. Further studies demonstrated the tunable emission of Ba_2ZnS_3: Ce, Eu in conjunction with blue LEDs, showcasing its utility in generating diverse white light sources [16]. Additionally, the red-emitting phosphor Ba_2ZnS_3: Eu^{2+}, when co-doped with halide ions, exhibited a remarkable green-to-red conversion, presenting promising opportunities for solar energy utilization [17]. It is plausible to anticipate similar luminesce properties in Sr_2ZnS_3. Chi-Woo Lee et al. observed that the substitution of Sr into the Ba site of Ba_2ZnS_3 leads to a significant enhancement of the fluorescence quantum efficiency accompanied by the blue shift of the emission peak, resulting in the bright orange–red emission from the material [18].

Thomas Mathew et al. studied the electronic and optical properties of Zinc based quasi-1D chalcogenides Ba_2ZnX_3 (X = S, Se, Te), which exhibit a wide band gap nature and are suitable for optoelectronic applications [4]. The results also highlight the fact that increasing the anionic radius enlarges the unit cell volume and decreases the band gap when transitioning from S to Se, Te. Several results from the literature show similar observations[3,4,19]. The latter observation motivates studying the physical properties of Sr_2ZnX_3 materials and determining their suitability for an application. Currently, there are no experimental crystal structure reports available for the Sr_2ZnSe_3 and Sr_2ZnTe_3 materials. In this study, both materials were constructed by substituting Se and Te for S in the Sr_2ZnS_3 crystal structure. The structure was then optimized using a GGA-PBE functional, with detailed criteria provided in Section 3.1. The optimized structure and its volume expansion are in good agreement with the previous results of similar isostructural materials [3,4].

In the current research, we have investigated the structural, electronic, optical, and thermoelectric properties of quasi-one-dimensional ternary chalcogenides Sr_2ZnX_3 materials using density functional theory with various approximations. While the structural properties of Sr_2ZnS_3 are known from a few experimental works; the electronic, optical, and thermoelectric properties remain unexplored via both experimental and theoretical approaches. Hence, the necessity of theoretical predictions to understand their suitability is crucial for desired applications. We perform structural optimization of novel Sr_2ZnSe_3 and Sr_2ZnTe_3 using the GGA-PBE functional, aligning with the quasi-one-dimensional nature of the material shown along the *b*-axis. Electronic properties are calculated to predict the bandgap value, nature of the bandgap, and effective mass of electrons and holes. To ensure the accuracy of the bandgap value the well-known TB-mBJ exchange–correlation functional is utilized. In addition, the spin–orbit coupling(SOC) is incorporated and the effect of SOC is known in accurate bandgap prediction. Optical properties such as the real and imaginary parts of the dielectric function, refractive index, extinction coefficient, absorption coefficient, energy loss function, and reflectivity within the 0–10 eV (IR–Vis–UV) region are studied. Thermoelectric properties, crucial for assessing material utility in thermoelectric applications, including Seebeck coefficients, thermal conductivity, electrical conductivity, power factor, and figure of merit (ZT), are analyzed. In summary, the outcome of this study reveals the wide direct bandgap of Sr_2ZnS_3 (3.42 eV), which classifies it as an insulator, Sr_2ZnSe_3 (2.82 eV) and Sr_2ZnTe_3 (1.75 eV), acting as semiconductors. The favorable direct bandgap of 1.75 eV, with the large dielectric constant, high absorption coefficients reaching 10^6 cm^{-1} in the visible and UV regions, low reflectivity, and minimal energy loss, makes Sr_2ZnTe_3 emerge as a potential candidate for photovoltaic applications. Furthermore, the wide bandgap of Sr_2ZnX_3 materials with a direct bandgap, lower effective mass, higher mobility, and significant optical and thermoelectric properties, indicates the suitability of Sr_2ZnX_3 materials for light-emitting semiconductors and thermoelectric applications [4,19].

Table 1
Optimized lattice parameters and cell volume of Sr_2ZnX_3 (X = S, Se, Te).

	a(Å)	*b*(Å)	*c*(Å)	V (Å)^3
Sr_2ZnS_3	8.51	4.09	16.50	575.72
	8.45	4.06	16.40	564.44[a]
Sr_2ZnSe_3	8.89	4.27	17.24	655.59
Sr_2ZnTe_3	9.52	4.58	18.46	806.01

[a] Represents the experimental lattice parameters and cell volume.

2. Computational methods

Ab initio computations employing the FP-LAPW (Full Potential Linear Augmented Wave) method was implemented in the WIEN2k code [20,21]. In our investigations, we have carried out self-consistent calculations to solve the Kohn–Sham equations [22], utilizing the Generalized Gradient Approximation and the Perdew–Burke–Ernzerhof (GGA-PBE) [23] as the exchange–correlation functional. The structural optimization was carried out, ensuring that the Hellmann–Feynman forces remained below 10^{-3} Ry/au and energy convergence criteria of 10^{-6} Ry were met for achieving the equilibrium structure, using the GGA-PBE functional with Van der Waals corrections. Accurate calculations were ensured by utilizing a substantial number of precise plane waves (PWs), and the facilitation of this precision was accomplished by setting $R_{MT} \times K_{max} = 8$. Where, K_{max} corresponds to the maximum reciprocal lattice vector utilized in the expansion of plane waves, whereas R_{MT} indicates the minimum radius of the smallest muffin-tin (MT) sphere. Integration of the Brillouin zone was conducted with 1000 k-points for Sr_2ZnX_3 materials. To elucidate the electrical and optical properties, the TB-mBJ [24] method, incorporating spin–orbit coupling (SOC), was employed, while Van der Waals corrections were introduced using Grimme's DFT-D3 method with Becke–Jonson damping. The BoltzTraP [25] package was utilized to determine the Boltzmann transport characteristics, such as electrical conductivity, Seebeck coefficient, and electronic thermal conductivity, employing the relaxation time approximation (RTA), where charge carriers are assumed to return to their ground states linearly with a lifetime of 10^{-14} seconds.

3. Results and discussion

3.1. Structural properties

Sr_2ZnX_3 (X = S, Se, Te) exhibits four structured formula units in the unit cell as shown in Fig. 1. X-ray diffraction analysis was conducted by V. Petrykin et al. to examine the crystal structure of Sr_2ZnS_3. The results confirmed an orthorhombic structure in the D_{2h}^{16} – Pnma space group [10], with Sr_2ZnS_3 exhibiting isostructural features similar to K_2AgI_3 [26], Ba_2ZnX_3 (X = S, Se, Te) [27], Ba_2MnSe_3 and Ba_2MnS_3 [28]. To attain the equilibrium structural properties, including lattice parameters and cell volume, we utilized the GGA-PBE exchange–correlation functional for full relaxation. The optimization process continued until the Hellmann–Feynman forces reached values smaller than 10^{-3} Ry/au, and the energy convergence criteria were achieved at 10^{-6} Ry. As the studied materials exhibit a quasi-one-dimensional nature, Van der Waals corrections were integrated using the DFT-D3 method with Becke–Jonson damping, proposed by Grimme [29].

The optimized lattice parameters and cell volume is listed in Table 1. The results depicted that lattice parameters and cell volume have increased from S (1.84) to Se (1.98) and Te (2.22) for Sr_2ZnX_3, which may be attributed to an increase in ionic radius (values in brackets denote the ionic radius of each element). The results are consistent with earlier observations regarding the influence of ionic radius on cell volume [3,30,31]. Specifically, we observed a 14% of volume change when composition changed from S-Se, and 40% from S-Te. The

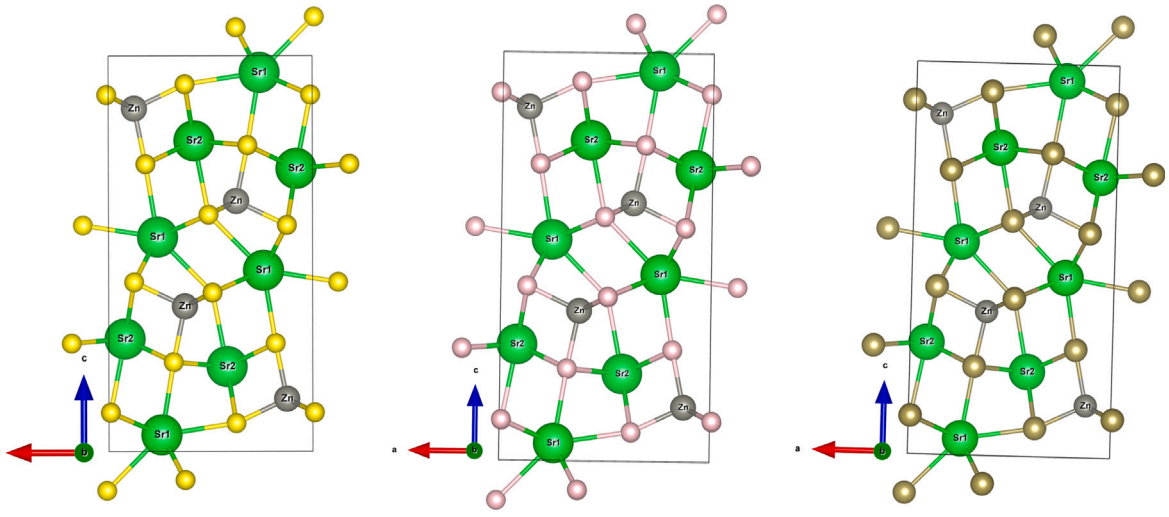

Fig. 1. Optimized structure of (a) Sr_2ZnS_3, (b) Sr_2ZnSe_3, and (c) Sr_2ZnTe_3 in a unit cell, each containing four formula units. Presented with yellow, pink, and algae green spheres representing S, Se, and Te atoms, respectively.

Table 2
Zn coordination in Sr_2ZnX_3: Bond lengths and Bond angles.

Bond	Bond length (Å)		
	Sr_2ZnS_3	Sr_2ZnSe_3	Sr_2ZnTe_3
Zn - X1	2.37	2.47	2.65
Zn - X2	2.42	2.52	2.71
Zn - X3	2.34	2.44	2.62
Zn - Zn	4.09	4.27	4.58
Angles (°)	Sr_2ZnS_3	Sr_2ZnSe_3	Sr_2ZnTe_3
X2 - Zn - X2	115.63	115.82	116.05
X3 - Zn - X2	109.24	109.49	109.76
X3 - Zn - X1	104.08	104.26	104.63
X1 - Zn - X2	109.00	109.28	109.53

Table 3
Sr coordination in Sr_2ZnX_3: Bond lengths and Bond angles.

Bond	Bond length (Å)		
	Sr_2ZnS_3	Sr_2ZnSe_3	Sr_2ZnTe_3
Sr1 - X1	3.07	3.21	3.44
Sr1 - X2	3.09	3.23	3.46
Sr1 - X3	2.95	3.08	3.30
Sr1 - X2[a]	3.26	3.40	3.65
Angles (°)	Sr_2ZnS_3	Sr_2ZnSe_3	Sr_2ZnTe_3
X2 - Sr1 - X2	82.81	82.97	83.14
X3 - Sr1 - X3	87.85	87.94	88.03
X1 - Sr1 - X2	79.39	79.52	79.76
X1 - Sr1 - X3	71.69	71.83	71.91
X2[a] - Sr1 - X3	77.15	77.27	77.43
X2[a] - Sr1 - X2	74.44	74.57	74.76

[a] Represents capped S2 atom positioned at top of the SrS_7 geometry.

optimized structures of Sr_2ZnX_3 are illustrated in Fig. 1. Additionally, the optimized cell volume versus energy curve, demonstrating the minimum energy curve for Sr_2ZnX_3 materials, is presented in Supplementary Figure S1. Fig. 2(f) presents a perspective view of the Sr_2ZnS_3 material, emphasizing the presence of infinite chains of ZnS_4 tetrahedra along the *b*-axis. The chains are separated by two crystallographically distinct Sr atoms that reside within the unit cell, further highlighting the quasi-one-dimensional nature of Sr_2ZnX_3 materials shown along the *b*-axis.

The unit cell contains three distinct sulfur atoms, Zn^{2+} coordinated with one identical S1, S3 anions, and two identical S2 anions to form a distorted tetrahedron. The bond length of Zn-X varies from 2.34 Å to 2.42 Å for ZnS_4, 2.44 Å to 2.52 Å for $ZnSe_4$, and 2.62 Å to 2.71 Å for $ZnTe_4$, respectively. Deviations from the ideal bond angle of 109.47° lead to the distortion of the tetrahedral geometry [2]. We observe the distorted tetrahedron with bond angle ranging from 109° to 115.63° for ZnS_4, and illustrates the deviation from the perfect tetrahedron, which is as shown in Fig. 2(d). Corner-sharing ZnS_4 tetrahedra and local coordination of Zn-S-Zn are shown in Fig. 2(e). The distance between two identical Zn atoms varies depending on the type of X, with values of 4.09 Å for Sr_2ZnS_3, 4.27 Å for Sr_2ZnSe_3 and 4.58 Å for Sr_2ZnTe_3. Detailed bond lengths and bond angles of Zn coordination are listed in Table 2.

The coordination number of the Sr^{2+} cation in Sr_2ZnX_3 materials is 7, with seven S^{2-} anions coordinating with the Sr^{2+} cation to form a capped trigonal prismatic geometry, as shown in Fig. 2(a). The Sr-S bond distances vary between 2.95 Å and 3.26 Å, with the longest bond length of 3.26 Å is observed for the capped S2 atom. The detailed bond lengths and angles of SrX_7 (X = S, Se, Te) coordination are tabulated in Table 3. In Fig. 2(f), two distinct Sr atoms are positioned between ZnS_4 chains. Sr1 and Sr2 are coordinated with three identical S2 and S3 atoms, along with one S1 atom, to form an edge-sharing capped trigonal prismatic structure. Figs. 2(b) and 2(c) depict the coordination environment, illustrating edge sharing between capped trigonal prismatic structures with Sr1-Sr2 and Sr1-Sr1.

3.2. Electronic properties

The optimized structures of Sr_2ZnX_3 materials are utilized to compute the band structure by incorporating the GGA-PBE exchange–correlation functional (XC), revealing their direct bandgap semiconductor nature with a wide bandgap. Spin–orbit coupling (SOC) plays a significant role in obtaining accurate bandgap values, particularly for heavier elements [32,33]. In the present study, SOC is incorporated with the PBE functional, resulting in an increased effect from S to Te, as the size of the anion increases. The bandgap values appear to decrease accordingly, as indicated in Table 4. The band structures of Sr_2ZnX_3 materials were plotted both with and without SOC, as depicted in supplementary Figure S2, revealing a notable shift in the conduction band curve towards lower energy levels, with a more pronounced effect observed in Sr_2ZnTe_3 material due to its larger ionic radius.

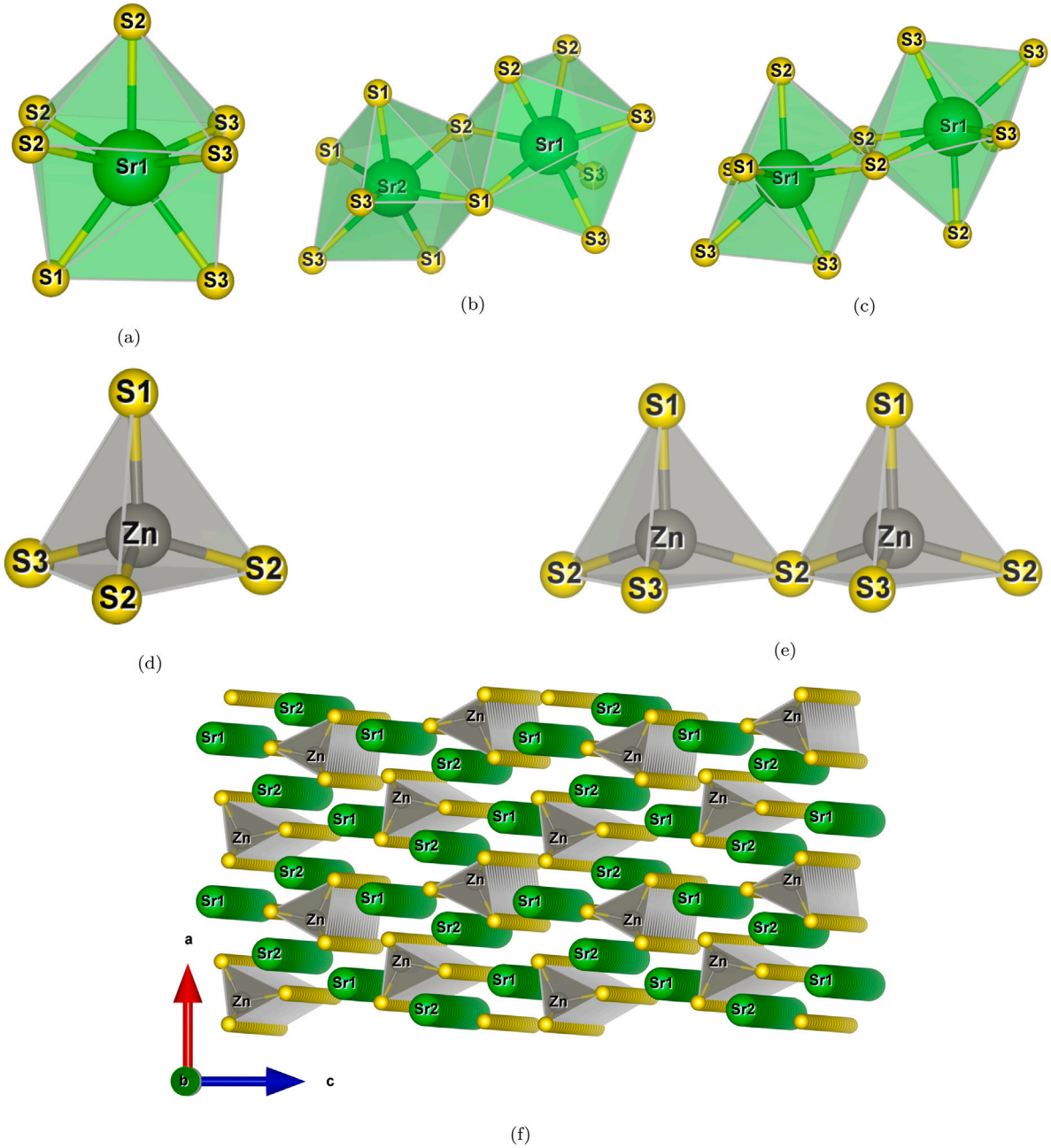

Fig. 2. Representation of local coordination environment for Sr_2ZnS_3: (a) Coordination of Sr with seven S anions forming capped trigonal prismatic (SrS_7) geometry, (b) Edge sharing between two distinct Sr1-Sr2 in SrS_7 geometry, (c) Edge sharing between two identical Sr1-Sr1 in SrS_7 geometry, (d) Zn coordinated with four S anions forming distorted tetrahedra, (e) Corner sharing ZnS_4 tetrahedra representing Zn-S-Zn coordination, (e) Perspective view representing ZnS_4 tetrahedra extended along *b*-axis highlighting the quasi-one-dimensional nature of Sr_2ZnS_3 materials.

However, several findings in the literature suggest that the PBE functional often underestimates the band gap value [3,34]. To address this limitation, we have utilized the TB-mBJ functional, which is well-regarded for its accuracy in determining electronic structures in solid-state systems [21,35]. Since we noticed a pronounced SOC effect with PBE functional, SOC is also incorporated with TB-mBJ functional. Figs. 3(a)–3(c) illustrate the calculated electronic band structures of Sr_2ZnX_3 materials, along with high symmetry points of the reciprocal lattice [36]. A horizontal straight line indicates the Fermi level, which represents zero energy. The computed bandgap values using TB-mBJ functional are 3.42 eV for Sr_2ZnS_3, 2.82 eV for Sr_2ZnSe_3, and 1.75 eV for Sr_2ZnTe_3, respectively, indicating the wide bandgap semiconducting nature of the material. As there are no reported experimental studies on the electronic properties of Sr_2ZnX_3 materials, a direct comparison with experimental data for the obtained band gap values is not feasible. However, the findings are in consistent with reports on similar isostructural ternary chalcogenide materials [4].

The band structure of Sr_2ZnX_3 materials reveals a pronounced dispersion in both valence and conduction bands, resulting in lower effective mass and higher carrier mobility. This enhances efficiency in applications like solar cells, where improved carrier mobility facilitates better transport of charge carriers, leading to enhanced device performance [37]. The effective masses of electrons and holes were determined using a second-order polynomial fit on the E(k) curve within the k-space for the conduction and valence bands [38]. Table 5 shows the computed relative effective masses of electrons (m_e^*) and holes (m_h^*) for Sr_2ZnX_3 ternary chalcogenide materials at the Γ(gamma) point. Materials with lower effective mass are of significant interest

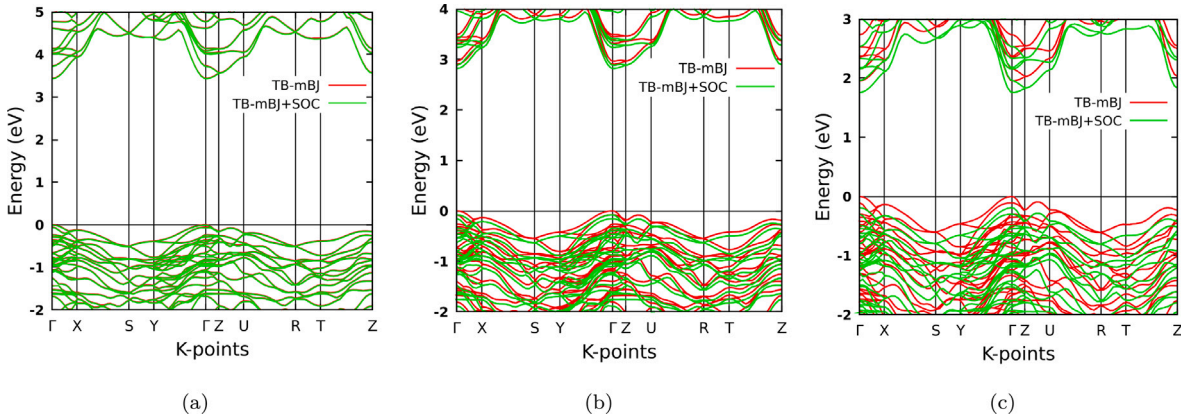

Fig. 3. Computed band structure of (a) Sr_2ZnS_3, (b) Sr_2ZnSe_3, and (c) Sr_2ZnTe_3 along the high symmetry points.

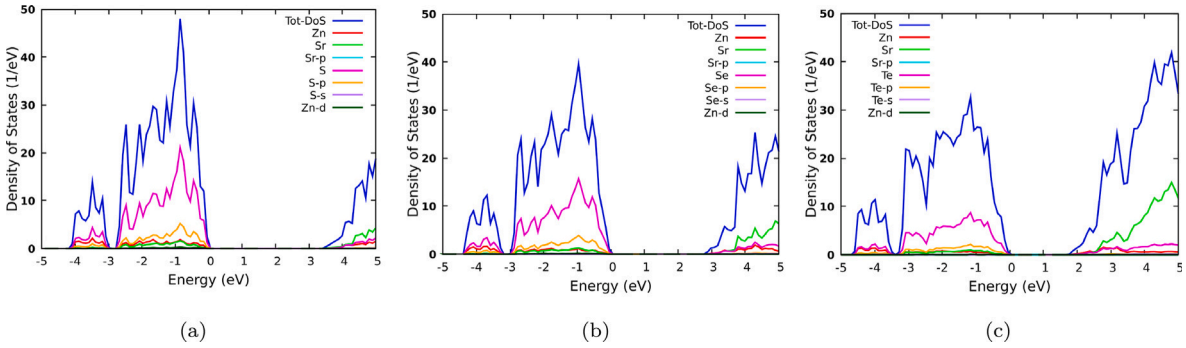

Fig. 4. The total and projected density of states: (a) Sr_2ZnS_3, (b) Sr_2ZnSe_3, and (c) Sr_2ZnTe_3 materials.

Table 4
Computed bandgap values of Sr_2ZnX_3 (X = S, Se, Te) materials from different approximation methods.

Materials	Bandgap (eV)			
	GGA-PBE	PBE+SOC	TB-mBJ	mBJ+SOC
Sr_2ZnS_3	2.409	2.395	3.437	3.425
Sr_2ZnSe_3	1.709	1.619	2.901	2.820
Sr_2ZnTe_3	1.220	1.020	1.952	1.757

Table 5
The effective mass of electrons and holes for Sr_2ZnX_3 (X = S, Se, Te) materials relative to the free electron mass.

Materials	m_e^*/m_o	m_h^*/m_o	m_h^*/m_e^*
Sr_2ZnS_3	0.14	−0.43	−3.07
Sr_2ZnSe_3	0.19	−0.25	−1.31
Sr_2ZnTe_3	0.16	−0.19	−1.18

in research due to their tendency to increase mobility, following the Bardeen–Shockley theory of deformation potential [39]. The obtained values (See Table 5) reveal that smaller effective masses of electrons and holes at the conduction band minima and valence band maxima lead to increased carrier mobility and diffusion [40,41]. The rates of charge recombination (expressed as $D = m_h^*/m_e^*$) exhibit substantial values of 3.07 for Sr_2ZnS_3, 1.31 for Sr_2ZnSe_3, and 1.18 for Sr_2ZnTe_3, respectively. Furthermore, this feature makes it easier to separate photogenerated charges efficiently, leading to a high absorption coefficient (around 10^5 cm^{-1}) in the visible and ultraviolet light regions, making it desirable for photovoltaic applications [42].

Figs. 4(a)–4(c) illustrates the computed total density of states and projected orbital density of states of the Sr_2ZnX_3 ternary chalcogenide materials, utilizing the TB-mBJ functional with SOC to gain a comprehensive understanding of their electronic structure. The analysis of density of states provides insights into the contribution of atomic orbitals in CBM and VBM, which helps researchers to predict and tune the band gap of the materials. The density of states analysis clearly shows that the valence band maxima are mainly dominated by X = S, Se, and Te chalcogenides, while the conduction band is significantly influenced by the hybridization of Sr and X atoms. The X-p orbitals have major contributions in both CBM and VBM, as compared to other orbital projections. Furthermore, the effect of ionic radius on the density of states is noticeable in the Figs. 4(a)–4(c). The intensity of the total density of states decreases in the valence band maxima as the ionic radius increases from S to Te, and a similar observation has been noticed in the atomic orbital projection of X to the total density of states.

3.3. Optical properties

Understanding optical behavior is crucial for describing potential optoelectronic applications. This involves interpreting how materials respond to incoming radiation, leading to electronic transitions across the Fermi level from the filled valence band to available states in the conduction band. In typical semiconductors, inter-band transitions from the valence to the conduction band are prevalent, while intra-band transitions play a significant role in metals [43]. In this study, we focus on evaluating the optical properties by considering the predominant interband contribution in semiconductors. A crucial component in evaluating the optical characteristics of materials is the complex dielectric function $\varepsilon(\omega)$, which is defined by Eq. (1) [44]. It describes the energy-dependent response of a material to electromagnetic radiation. In addition, the optical properties have been calculated and analyzed using the real and imaginary components of the complex dielectric function, and determined the refractive index, extinction coefficient,

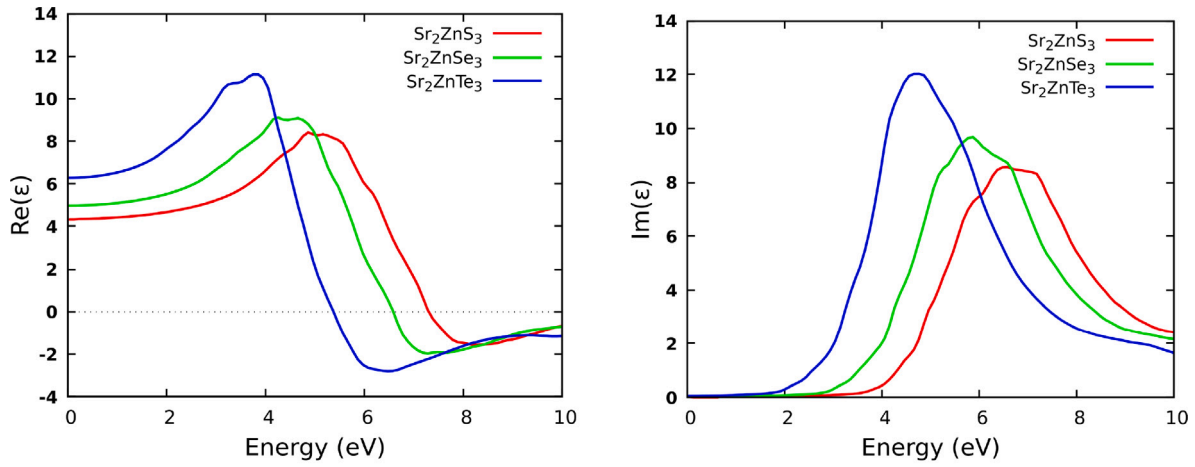

Fig. 5. Frequency response plots of isotropic average dielectric function of Sr_2ZnX_3 materials with incident photon energies: (a) real dispersive part, and (b) absorptive imaginary part.

absorption coefficient, energy loss function, and reflectivity across the photon energy range of 0 to 10 eV.

$$\varepsilon(\omega) = \varepsilon^{(1)}(\omega) + i\ \varepsilon^{(2)}(\omega) \tag{1}$$

$$\varepsilon^{(2)}_{\alpha,\beta} = \frac{4\pi^2 e^2}{\Omega} \lim_{q\to 0} \frac{1}{q^2} \sum_{c,v,\mathbf{k}} 2w_{\mathbf{k}} \delta(\epsilon_{c,\mathbf{k}} - \epsilon_{v,\mathbf{k}} - \omega) \times \langle u_{c,\mathbf{k}+e_\alpha q} | u_{v,\mathbf{k}} \rangle \langle u_{c,\mathbf{k}+e_\beta q} | u_{v,\mathbf{k}} \rangle^* \tag{2}$$

The relationship between a material's electronic structure, interband transitions, and optical properties is described in Eq. (2). Here, ε_k refers to the energy eigenvalues associated with the system, u_k for the cell periodic Bloch function, ω_k are the weights of the k-points that sum to 1, e_α represents unit vectors along the principal directions of the crystal, q for the wave vector of the incoming radiation, and Ω for the primitive cell volume. It is possible to extract the real component $\varepsilon^{(1)}$ and the imaginary component $\varepsilon^{(2)}$ of the complex parameter ε by the Kramers–Kronig transformation [45]. The imaginary component of the dielectric functions $\varepsilon^{(2)}$ is calculated by considering the summation of transitions between the occupied (α) and unoccupied (β) states within the Brillouin zone [46]. Further, taking into account the spin degeneracy of both conduction and valence band states, the imaginary part of the dielectric tensor $\varepsilon^{(2)}$ is determined by Eq. (2). The real component is obtained by using the Kramers–Kronig transformation [45], as presented by Eq. (3).

$$\epsilon^{(1)}_{\alpha,\beta} = 1 + \frac{2}{\pi} P \int_0^\infty \frac{\epsilon^{(2)}_{\alpha,\beta}(\omega')\omega'}{\omega'^2 - \omega^2 + i\eta} d\omega' \tag{3}$$

The dielectric constant, referred to as the relative permittivity, is a material property that measures its ability to polarize when exposed to an electric field. A higher dielectric constant means the material can store more energy per unit volume. This property has important uses, particularly in capacitors, where dielectric materials enhance energy storage capacity [47]. In addition, the dielectric constant affects how electromagnetic waves behave when they propagate through a material, influencing the waves' reflection and refraction as well as other characteristics like wave velocity. The dispersion of incident photons is characterized by the real component ($\varepsilon^{(1)}$) of the dielectric function, which also reveals the refractive behaviors of the material by demonstrating how its refractive index varies with the frequency of light. Conversely, the imaginary component ($\varepsilon^{(2)}$) is concerned with light absorption by the material [48].

Figs. 5(a) and 5(b) depicts the dispersive real part $\varepsilon^{(1)}$ and the absorptive imaginary part $\varepsilon^{(2)}$ of the dielectric function for Sr_2ZnX_3 materials with an incident photon energy range from 0 to 10 eV. The onset dielectric function, referring to the dielectric constant at zero frequency, is 4.35 for Sr_2ZnS_3, 4.98 for Sr_2ZnSe_3, and 6.28 for Sr_2ZnTe_3, respectively. The onset dielectric function is a crucial parameter since it is directly related to the semiconductor bandgap of the materials, as given by the Penn model [49,50]. Furthermore, as observed from Fig. 5(a), $\varepsilon^{(1)}$ increases with the increase in energy and attains a maximum value of 8.34 at 5.15 eV for Sr_2ZnS_3, 9.25 at 4.35 eV for Sr_2ZnSe_3, and 11.46 at 3.79 eV for Sr_2ZnTe_3 materials, respectively. Beyond this energy range, a steep decrease has been observed, followed by a negative state, reaching its minimum value, and then gradually rising towards zero at higher energy levels. The range of input photon energies where the real part of the dielectric function $\varepsilon^{(1)} < 0$ indicates the forbidden region for electromagnetic wave propagation [46,51]. Notably, in the range of 0–10 eV, Sr_2ZnTe_3 possesses the largest forbidden region for incident photon energies among these materials, followed by Sr_2ZnSe_3 and Sr_2ZnS_3. We observe an increase in the dielectric function across the infrared, visible, and near-UV regions, with Sr_2ZnTe_3 displaying a higher dielectric constant compared to the other materials under study. As discussed earlier, materials with larger dielectric constants are preferable for optoelectronic applications [48].

The optical characteristics of materials, including the extinction coefficient, absorption coefficient, energy loss function, and reflectivity, are predominantly defined by the imaginary component of the complex dielectric function $\varepsilon^{(2)}$ [3]. The imaginary part of the dielectric function $\varepsilon^{(2)}$ for Sr_2ZnX_3 materials, intricately connected to the process of photon absorption, is depicted in Fig. 5(b). The threshold point for the onset of rising $\varepsilon^{(2)}$ is observed at around 3.48 eV for Sr_2ZnS_3, 2.81 eV for Sr_2ZnSe_3, and 1.87 eV for Sr_2ZnTe_3, respectively. This observation is nearly comparable to the bandgap of the materials, and signifies the direct transition from the valence band maximum to the conduction band minimum, which is responsible for the rise in the imaginary part of the dielectric function. A sharp increase in $\varepsilon^{(2)}$ is observed with increased energy, reaching a maximum value of 8.55 at 6.54 eV for Sr_2ZnS_3, 9.73 at 5.73 eV for Sr_2ZnSe_3, and 12.34 at 4.49 eV for Sr_2ZnTe_3, respectively. The largest values of $\varepsilon^{(2)}$ for Sr_2ZnX_3 exhibit around the UV (> 3.1 eV) region, implying strong interband transitions and thus potential for superior optical absorption, making it suitable for photovoltaic applications. The observed shift of peaks to lower energy levels from S to Se to Te underscores the impact of ionic radius on the material's dielectric function. The significant decrease in $\varepsilon^{(1,2)}$ observed during the transition from tellurium (Te) to selenium (Se) to sulfur (S) can be attributed to the: (1) inverse relationship between the optical

bandgap and the optical dielectric response, and (2) ionic dielectric response, which is typically lower in compounds with lighter elements due to their faster vibrations [52,53].

To explore the anisotropic behavior of the dielectric function, the values of $\varepsilon^{(1)}(\omega)$ and $\varepsilon^{(2)}(\omega)$ along distinct crystal directions as a function of energy for Sr_2ZnX_3 materials are plotted. The anisotropic plots are displayed in Supplementary Materials, Figs. 3S(a–f) for Sr_2ZnX_3. Specifically, $\varepsilon_{xx}^{(1,2)}$, $\varepsilon_{yy}^{(1,2)}$ and $\varepsilon_{zz}^{(1,2)}$ defines the dielectric function along xx, yy, and zz direction. Figs. 3S(a–c) depicts the components of the real part of the dielectric function, and Figs. 3S(d–f) represent the imaginary part, along different directions for Sr_2ZnS_3, Sr_2ZnSe_3, and Sr_2ZnTe_3, respectively. Notably, the onset dielectric constant exhibits a slightly larger magnitude along the yy direction for all the materials studied, and the relevant data are presented in Table 6. Figures 3S(a–c) depict the anisotropy plots of the real part of the dielectric function $\varepsilon^{(1)}$ for Sr_2ZnX_3. The materials exhibit almost isotropic behavior in the visible and infrared ranges up to 3.1 eV. With further increasing energy, slight anisotropy emerges after 3.3 eV for Sr_2ZnTe_3, 3.8 eV for Sr_2ZnSe_3, and 4.2 eV for Sr_2ZnS_3, respectively. The dielectric function further varies across distinct directions, with $\varepsilon^{(1)}$ sharply rising and attaining the maximum value along the yy direction. Notably, as energy further increases, a sudden decline in the dielectric function occurs, with $\varepsilon^{(1)}$ reaching negative values, indicating negative dielectric constants, signifying the forbidden region for electromagnetic waves. A similar observation is noted regarding the imaginary part of the dielectric function: the anisotropy is almost negligible up to the threshold energy limit (equivalent to the bandgap of the material), after which noticeable anisotropy is observed along different directions for all the studied materials.

The imaginary component of the complex refractive index, known as the extinction coefficient (k), represents energy dissipation within the material. While the real component refractive index (n) characterizes light-bending behavior. Applying the Kramers–Kronig transfor mation yields the frequency-dependent extinction coefficient k as follows [54]:

$$k = \sqrt{\frac{\left[\left(\varepsilon^{(1)}\right)^2 + \left(\varepsilon^{(2)}\right)^2\right]^{1/2} - \varepsilon^{(1)}}{2}} \tag{4}$$

the real component n is described by Eq. (5).

$$n = \sqrt{\frac{\left[\left(\varepsilon^{(1)}\right)^2 + \left(\varepsilon^{(2)}\right)^2\right]^{1/2} + \varepsilon^{(1)}}{2}} \tag{5}$$

The determination of the static refractive index at the zero-frequency limit, denoted as n(0), is accomplished by utilizing the static dielectric function $\varepsilon^{(1)}(0)$ [55] as provided in Eq. (6).

$$\mathrm{n}(0) = \sqrt{\varepsilon^1(0)} \tag{6}$$

The phase velocity of light within a medium of electromagnetic waves is determined by the real part of the refractive index (n). Understanding the refractive index value is crucial when evaluating materials suitability for optical instrument applications. The variation of the refractive index within the range of 0–10 eV is depicted in Fig. 6(a). The n(0), known as the onset refractive index along distinct directions, and its isotropic average for Sr_2ZnX_3 material are tabulated in Table 6. The value of n increases as the energy increases and reaches maximum values of 2.97 for Sr_2ZnS_3, 3.14 for Sr_2ZnSe_3, and 3.52 for Sr_2ZnTe_3, respectively, in the UV region. The peaks of n undergo significant shifts towards lower energies when the anions change from S to Se, and Te. Notably, the static refractive indices increase from Sr_2ZnS_3 to Sr_2ZnTe_3. This trend is also observed in analogous chalcogenide ternary materials such as Ba_2CdX_3 [3] and Ba_2ZnX_3 [4], with X varying from S to Te. At higher energies, the value of the refractive index is observed to be less than one, indicating the forbidden regions for electromagnetic waves.

Table 6
Computed Components of the dielectric function, refractive index and reflectivity of Sr_2ZnX_3 materials.

Dielectric function	$\varepsilon_{xx}^{(1)}(0)$	$\varepsilon_{yy}^{(1)}(0)$	$\varepsilon_{zz}^{(1)}(0)$	$\varepsilon^{(1)}(0)$
Sr_2ZnS_3	4.34	4.37	4.34	4.35
Sr_2ZnSe_3	4.97	4.99	4.97	4.98
Sr_2ZnTe_3	6.27	6.29	6.27	6.28
Refractive index	$n_{xx}(0)$	$n_{yy}(0)$	$n_{zz}(0)$	$n(0)$
Sr_2ZnS_3	2.08	2.09	2.08	2.08
Sr_2ZnSe_3	2.22	2.23	2.23	2.23
Sr_2ZnTe_3	2.50	2.51	2.50	2.50
Reflectivity	$R_{xx}(0)$	$R_{yy}(0)$	$R_{zz}(0)$	$R(0)$
Sr_2ZnS_3	0.12	0.12	0.12	0.12
Sr_2ZnSe_3	0.14	0.14	0.14	0.14
Sr_2ZnTe_3	0.18	0.18	0.18	0.18

The imaginary component of the complex refractive index (k), is associated with a material light absorption, determining its opacity or transparency. A higher value of k signifies increased light absorption, thereby reducing the material's transparency at that specific frequency. Fig. 6(b) represents the variation of k with incident photon energy. Up to the optical cutoff region, all the materials studied have nearly zero k values (transparency region); further increase in energy results in a gradual rise in k values, reaching maximum values of 1.96 for Sr_2ZnS_3, 2.15 for Sr_2ZnSe_3, and 2.4 for Sr_2ZnTe_3, respectively (higher absorption region). Furthermore, the k value decreases at very high frequencies due to weak absorption. The extinction coefficient (k), is associated with the decay or damping of the oscillation amplitude of the incident electric field. It exhibits behavior analogous to the absorption coefficient (α), as they are related through the Beer–Lambert law [56].

The determination of optical absorption coefficient (α), reflectivity (R), and energy loss function (L), is derived from the dielectric function using the following Eqs. (7), (8), and (9), respectively.

$$\alpha = \frac{2\omega}{c}k \tag{7}$$

$$R = \frac{[n-1]^2 + k^2}{[n+1]^2 + k^2} \tag{8}$$

$$L = \frac{\epsilon^{(2)}}{(\epsilon^{(1)})^2 + (\epsilon^{(2)})^2} \tag{9}$$

Fig. 7(a) illustrates the spectrum of the absorption coefficient (α) for Sr_2ZnX_3 materials, explaining how light is absorbed by them. It is vital to note that the energy band gap Eg has a substantial influence on the calculated optical characteristics [48]. Absorption occurs at threshold energies, corresponding to optical bandgaps of 3.63 for Sr_2ZnS_3, 2.89 for Sr_2ZnSe_3, and 1.97 for Sr_2ZnTe_3, respectively, indicating transparency up to these points. The obtained values for optical edges align well with the computed bandgap values from the band structure. Notably, all materials studied exhibit maximum absorption at around 10^6 cm^{-1} in the UV region. Additionally, the peaks shift to lower energy levels from S to Te variation, highlighting the effect of ionic radius on the optical properties of the material. Sr_2ZnTe_3 material also demonstrates noticeable absorption of the order of 10^5 cm^{-1} in the visible region due to its lower optical bandgap. Further, the high absorption coefficient of the studied materials, which is on the order of 10^6 cm^{-1} in the ultraviolet (UV) region, indicates their potential as UV absorbers suitable for integration into sensitive devices, photovoltaics, and other optoelectronic applications.

The reflectivity plots of Sr_2ZnX_3, as shown in Fig. 7(b), define the surface characteristics of the material. These plots illustrate the proportion of incident light that is reflected by the material across different regions of the electromagnetic spectrum. For the studied materials, the reflectivity is observed to be less than 20% in the IR region and 25% in the visible region, and the maximum value of reflectivity is found in the UV region, which is less than 0.4 (40%) for Sr_2ZnS_3 and Sr_2ZnSe_3

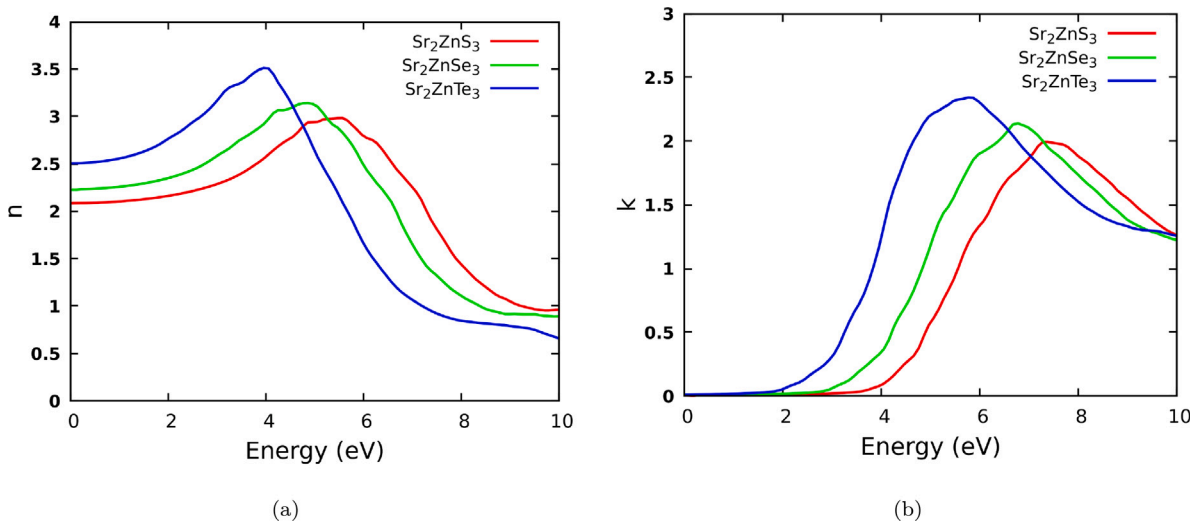

Fig. 6. Frequency response plots of isotropic average: (a) refractive index (n), and (b) extinction coefficient (k) of Sr_2ZnX_3 materials with incident photon energies.

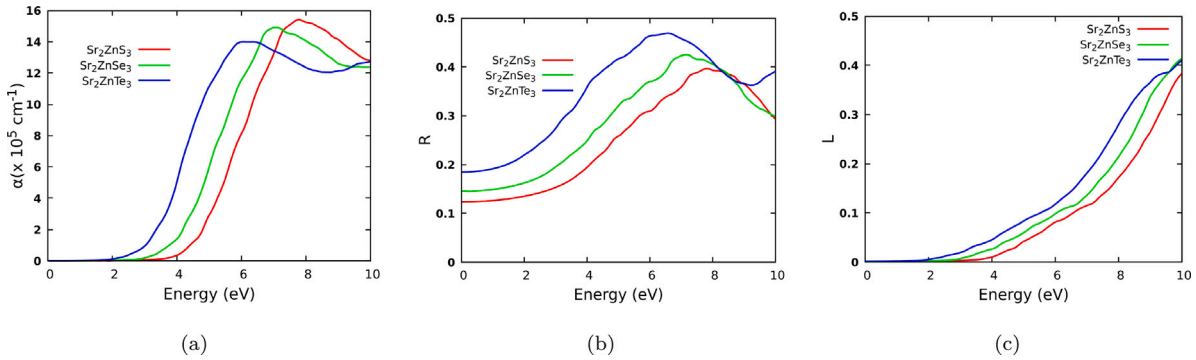

Fig. 7. Frequency response plots of isotropic average: (a) Optical absorption coefficient (α), (b) reflectivity (R), and (c) energy loss function (L) for Sr_2ZnX_3 materials with incident photon energies.

materials and 0.47 (47%) for Sr_2ZnTe_3 material, respectively. Fig. 7(c) illustrates the variation of the energy loss function (L) with incident photon energy. It describes the energy lost by electrons per unit length in a material when an incident electromagnetic beam penetrates it. The energy loss is observed to be almost nil till the optical band gap regions, as discussed earlier, which may be due to the transparent behavior of the materials. Notably, with further increase in energy, energy loss is likely to be increased, and we found the energy loss to be less than 0.1 in the visible region and less than 0.4 in the studied incident photon energy range of 0–10 eV.

3.4. Thermoelectric properties

Direct heat-to-electricity conversion is by far the quickest, least expensive, and most effective method of utilizing excess heat as energy. Seebeck coefficient (S), electrical conductivity (σ), thermal conductivity (k), and the figure of merit (ZT) are all valuable metrics for assessing material's suitability for thermoelectric applications [57]. Figs. 8(a) and 8(b) represent the variation of the electronic conductivity and Seebeck coefficient as a function of chemical potential. The chemical potential(μ) for electrons in semiconductor materials indicates the energy needed to add or remove electrons from the system. The Fermi level is set to zero in Figs. 8(a) and 8(b), which serves as a reference point that separates n-type (conduction band region) and p-type (valence band region) semiconductors. The electrical conductivity (σ/τ) measures a material's ability to conduct electric current. Fig. 8(a) illustrates the variation of (σ/τ) with chemical potential, whereas the maximum peak is observed in the positive chemical potential region for all the studied materials. Specifically, the peak intensities were observed at 14.0 for Sr_2ZnS_3, 13.4 for Sr_2ZnSe_3, and 10.8 for Sr_2ZnTe_3, respectively. Furthermore, the maximum peak intensities observed in the conduction band region (positive chemical potential region) signify the n-type semiconductor nature of Sr_2ZnX_3 materials. The temperature dependence of electrical conductivity is depicted in Fig. 8(c). As temperature increases, more charge carriers are thermally excited, resulting in enhanced electrical conductivity. This intricate relationship depends on the balance between the carrier concentration and the material's mobility. The plot in Fig. 8(c) illustrates the variation of electrical conductivity with temperature, clearly indicating an ascending trend for Sr_2ZnX_3 materials.

Seebeck coefficient measures the voltage generated across a material due to a temperature difference. The Seebeck coefficient in materials is influenced by several factors, including band structure, electronic density of states, carrier concentration, and mobility. Seebeck coefficient is directly connected to the behavior of charge carriers. Materials with a high Seebeck coefficient, charge carriers are more effectively transported in response to temperature differences, leading to efficient thermoelectric energy conversion [58]. Fig. 8(b) illustrates the variation of the Seebeck coefficient concerning chemical potential. Notably, the Seebeck coefficient exhibits a fluctuation, ranging from 1.5 mV/K to −1.5 mV/K within the specified chemical potential range of −1 eV to +1 eV. This behavior signifies the material's sensitivity to changes in chemical potential, indicating potential applications in thermoelectric systems. The determination of charge carrier type, whether p-type or n-type, can be deduced through the temperature-dependent behavior of the Seebeck coefficient. Fig. 8(d) illustrates the temperature

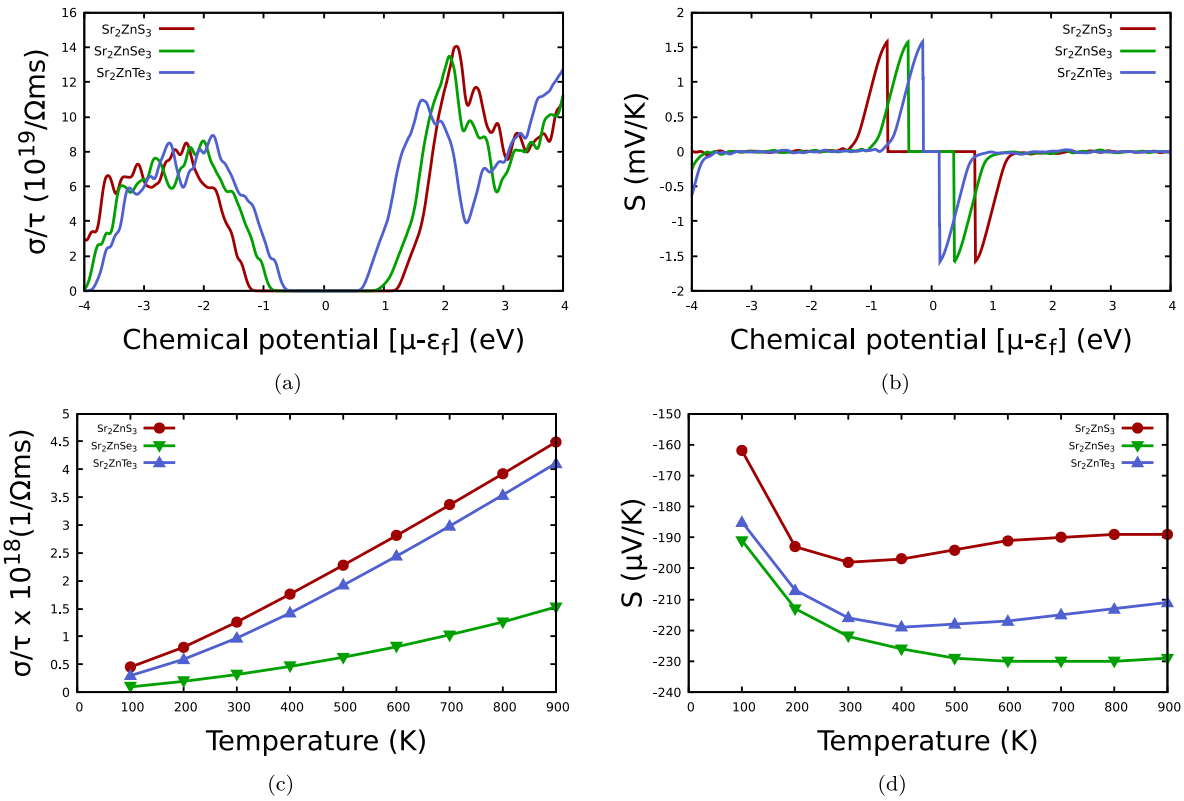

Fig. 8. Variation of electrical conductivity (σ/τ) and Seebeck coefficient concerning chemical potential and temperature.

variation of the Seebeck coefficient within the range of 100–900K. It is observed that the Seebeck coefficient consistently exhibits negative values across the entire temperature spectrum for Sr_2ZnX_3 materials. This negative polarity implies that the generated voltage's direction depends on the temperature gradient, indicative of Sr_2ZnX_3 materials n-type semiconductor nature.

Thermal conductivity in a material can occur through two modes: electron thermal conductivity (k_e) and phonon thermal conductivity (k_{ph}). The total thermal conductivity, k, is the sum of k_e and k_{ph}. However, the current calculations focus solely on electronic thermal conductivity due to the classical limitations in the BoltzTraP code [59]. The examination of thermal conductivity provides valuable insights. Fig. 9(a) illustrates the temperature-dependent variation of k_e/τ. From Fig. 9(a), it is evident that k_e/τ is nearly zero at low temperatures (100K), then gradually escalates with rising temperatures. The current observation underscores that higher temperatures enhance thermal conduction through free carriers [60]. Remarkably, all the materials studied exhibit low thermal conductivity below room temperature, measuring less than 10^{13} W/mKs. At room temperature, the computed values remain below 0.25×10^{13} W/mKs for Sr_2ZnX_3 materials, making them promising for thermoelectric (TE) applications due to their low thermal conductivity. However, as temperature increases, we notice that Sr_2ZnS_3 and Sr_2ZnTe_3 have higher thermal conductivity as compared to Sr_2ZnSe_3 materials. Fig. 9(a) showcases the variation of thermal conductivity concerning temperature, emphasizing the impact of electron conduction on the material's thermal properties. Further, the Weidman–Franz ratio (σ/k) falls within the range of 10^6 and provides evidence for the suitability of the materials in thermoelectric applications [61]. The persistent high ratio of electrical to thermal conductivity underscores the predominant role of electronic contribution in thermal conduction, while the impact of lattice vibrations is minimal at room temperature [62].

The thermoelectric figure of merit (ZT) is crucial for assessing a material's thermoelectric performance, representing its efficiency in converting heat into electricity. It is calculated using $ZT = S^2\sigma T/k$, where σ is electrical conductivity, S is the Seebeck coefficient, T is temperature, and k is thermal conductivity, respectively. A higher ZT value (greater than 1) indicates better thermoelectric efficiency, requiring a combination of factors that includes: a high Seebeck coefficient for robust voltage generation, low thermal conductivity to minimize heat loss, and high electrical conductivity for efficient charge carrier transfer, and further enhances power production [63]. Fig. 9(b) illustrates the variation of the calculated figure of merit with temperature. From the Fig. 9(b), it is evident that at a low temperature of 100K, Sr_2ZnSe_3(1.81) and Sr_2ZnTe_3(1.74) exhibit higher ZT values as compared to Sr_2ZnS_3(1.27). This observation aligns with the expectation due to their lower electrical conductivity and Seebeck coefficient, as discussed previously. At room temperature, all the materials in our study demonstrate ZT values greater than 2. Furthermore, they reach maximum values of 2.26 for Sr_2ZnS_3 at 500K, 2.58 for Sr_2ZnSe_3 at 400K, and 2.72 for Sr_2ZnTe_3 at 600K, respectively. As discussed earlier, achieving ZT values greater than 1 is a crucial factor for enhanced thermoelectric performance. This underscores the potential of Sr_2ZnX_3 materials for high-performance thermoelectric applications, facilitating the efficient conversion of heat into useful electrical energy. Such advancements contribute significantly to energy sustainability and heat recovery across various fields [64].

The Hall coefficient (R_H) is determined by dividing the induced electric field by the product of carrier density and the strength of the magnetic field; it is used to analyze a material's resistance in Hall geometry. The calculated R_H for the materials under study is illustrated in Fig. 9(c), showing a sudden decrease until 600K, followed by a nearly constant variation with temperature. The slight decrease in R_H at higher temperatures can be attributed to the increased thermal liberation of charge carriers in the material, leading to an enhancement in carrier mobility [65].

The power factor (PF) is a crucial parameter for thermoelectric power generation, which determines the strength of thermoelectric

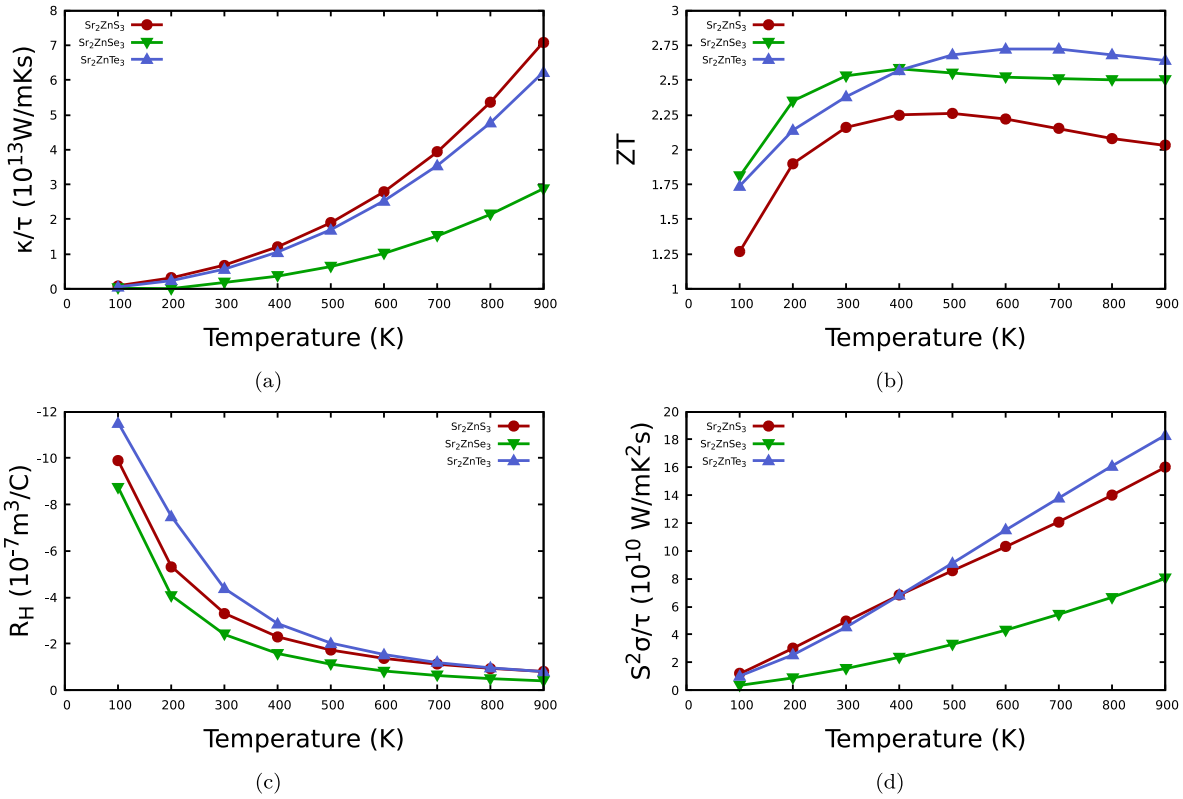

Fig. 9. Temperature-dependent thermoelectric characteristics of Sr_2ZnX_3 (X= S, Se, Te): (a) Thermal conductivity, (b) Figure of merit (ZT), (c) Hall coefficient (R_H), and (d) Power Factor.

materials and is calculated by using the following equation: $S^2\sigma/\tau$. The temperature-dependent variation of PF is depicted in Fig. 9(d). At room temperature, the examined materials exhibited power factor value of 4.94×10^{10} W/mK^{2}s for Sr_2ZnS_3, 1.56×10^{10} W/mK^{2}s for Sr_2ZnSe_3, and 4.53×10^{10} W/mK^{2}s for Sr_2ZnTe_3, respectively. Sr_2ZnSe_3 shows a comparatively lower value due to its lower Seebeck coefficient and electrical conductivity, as discussed earlier. The power factor shows an almost linear increase with rising temperature, reaching high values at higher temperatures for both Sr_2ZnS_3 and Sr_2ZnTe_3, attributing to the enhanced electrical conductivity as illustrated in Fig. 8(c). For Sr_2ZnSe_3, it gradually increases with temperature. The studied thermoelectric properties confirm that the Sr_2ZnX_3 materials exhibit n-type semiconductor nature, with considerable power factor and ZT values of Sr_2ZnX_3 (X = S, Se, Te), indicating their suitability for thermoelectric applications.

4. Conclusion

An investigation of Zn-based ternary chalcogenide Sr_2ZnX_3 (X = S, Se, Te) materials using density functional theory (DFT) revealed their structural stability and quasi-one-dimensional nature along the *b*-axis, consistent with similar isostructural materials. The effect of ionic radius in modulating physical properties is analyzed by constructing two novel Sr_2ZnSe_3 and Sr_2ZnTe_3 semiconductor materials. Band structure analysis is carried out to determine the electronic properties. We found that Sr_2ZnX_3 materials exhibit wide direct bandgaps, with Sr_2ZnS_3 (3.4 eV), Sr_2ZnSe_3 (2.8 eV), and Sr_2ZnTe_3 (1.75 eV), respectively. The lower effective mass of electrons and holes indicates the ability for higher carrier mobility and charge recombination rates, which is vital for photovoltaic applications. Optical properties, including dielectric function, refractive index, absorption, and reflectivity, are comprehensively analyzed across the 0–10 eV energy range (IR–Vis–UV). Sr_2ZnTe_3 material shows higher dielectric function values, absorption coefficient ($\alpha \approx 10^6$ cm^{-1}), refractive index, and lower reflectivity, which indicates its suitability for photovoltaic applications. Thermoelectric properties are crucial for assessing material utility in thermoelectric applications. Sr_2ZnX_3 materials exhibited n-type semiconductor nature with substantial values of the Seebeck coefficient, electrical conductivity, figure of merit (ZT) greater than 2, power factor, and lower electronic thermal conductivity. The direct bandgap, lower effective mass of electrons and holes, and significant optical and thermoelectric properties of the studied materials signify Sr_2ZnX_3 as potential candidates for light-emitting diodes and thermoelectric applications.

CRediT authorship contribution statement

Chethan V.: Writing – original draft, Visualization, Validation, Software, Methodology, Formal analysis, Conceptualization. **Mahendra M.:** Writing – review & editing, Validation, Supervision, Project administration, Investigation, Conceptualization.

Declaration of competing interest

The authors declare that they have no known competing financial interests or personal relationships that could have appeared to influence the work reported in this paper.

Data availability

Data will be made available on request.

Acknowledgments

The author Chethan V. thanks to University Grants Commission (UGC), New Delhi, India for providing financial support (NTA-Ref. No.: 211610131478, Dated: 19-04-2022). Dr. Mahendra M. would like to thank VGST, Government of Karnataka for awarding a research grant under the head K-FIST L2 (KSTePS/VGST/GRD No. 1133/2022–23/654).

Appendix A. Supplementary data

Supplementary material related to this article can be found online at https://doi.org/10.1016/j.jpcs.2024.112222.

References

[1] J. Gopalakrishnan, K. Nanjundaswamy, Transition metal chalcogenides exhibiting quasi-one-dimensional behaviour, Bull. Mater. Sci. 5 (1983) 287–306.

[2] W. Baur, The geometry of polyhedral distortions. Predictive relationships for the phosphate group, Acta Crystallogr. B: Struct. Crystallogr. Crystal Chem. 30 (5) (1974) 1195–1215.

[3] C. Sujith, S. Joseph, T. Mathew, V. Mathew, First-principles investigation of structural, electronic and optical properties of quasi-one-dimensional barium cadmium chalcogenides Ba2CdX3 (X= S, Se, Te) using HSE06 and GGA-PBE functionals, J. Phys. Chem. Solids 161 (2022) 110488.

[4] T. Mathew, C. Sujith, V. Mathew, et al., Electronic and optical properties of Quasi-1D barium zinc chalcogenides Ba2ZnX3 (X=S, Se, Te): A DFT approach, Solid State Sci. 113 (2021) 106456.

[5] W.-J. Chun, K. Asakura, Y. Iwasawa, Application of a cdte solid-state detector to polarization-dependent total-reflection fluorescence xafs measurements, J. Synchrotron Radiat. 3 (4) (1996) 160–162.

[6] G.F. Neumark, Defects in wide band gap II-VI crystals, Mater. Sci. Eng. R 21 (1) (1997) iii–46.

[7] N. Nakayama, K. Kosuge, S. Kachi, T. Shinjo, T. Takada, Studies on the compounds in the Ba2 Fe S3 system. I. Linear chain antiferromagnetism of Ba2FeS3 and related compounds Ba2CoS3 and Ba2MnS3, J. Solid State Chem. 33 (3) (1980) 351–356.

[8] M.D. Esrafili, S. Asadollahi, Y. Dadban Shahamat, Competition between chalcogen bond and halogen bond interactions in yox 4: NH 3 (Y=S, Se; X=F, Cl, Br) complexes: An ab initio investigation, Struct. Chem. 27 (2016) 1439–1447.

[9] M.D. Esrafili, F. Mohammadian-Sabet, Does single-electron chalcogen bond exist? Some theoretical insights, J. Molecular Model. 21 (2015) 1–9.

[10] V. Petrykin, M. Okube, H. Yamane, S. Sasaki, M. Kakihana, Sr2ZnS3: crystal structure and fluorescent properties of a New Eu (II)-activated yellow emission phosphor, Chem. Mater. 22 (21) (2010) 5800–5802.

[11] H.G. Schnering, R. Hoppe, Zur Kenntnis des Ba2ZnS3, Z. Anorganische Allgemeine Chemie 312 (1–2) (1961) 99–109.

[12] R. Scott, D. Nicholas, M. Shropshall, The growth of single crystals of Ba2ZnS3, J. Cryst. Growth 38 (2) (1977) 269–271.

[13] Y.-F. Lin, Y.-H. Chang, B.-S. Tsai, The influence of processing parameters on photoluminescent properties of Ba2ZnS3: Ce phosphors by double-crucible method, J. Alloys Compd. 377 (1–2) (2004) 277–282.

[14] X. Zhang, J. Wang, J. Zhang, Q. Su, Photoluminescence properties of Eu2+ doped Ba2ZnS3 phosphor for white light emitting diodes, Mater. Lett. 61 (3) (2007) 761–764.

[15] P. Thiyagarajan, M. Kottaisamy, M.R. Rao, Luminescent properties of near UV excitable Ba2ZnS3: Mn red emitting phosphor blend for white LED and display applications, J. Phys. D: Appl. Phys. 39 (13) (2006) 2701.

[16] W.-J. Yang, T.-M. Chen, Ce3+/ Eu2+ codoped Ba2ZnS3: A blue radiation-converting phosphor for white light-emitting diodes, Appl. Phys. Lett. 90 (17) (2007).

[17] T. Luo, Y. Du, Z. Qiu, Y. Li, X. Wang, W. Zhou, J. Zhang, L. Yu, S. Lian, Remarkably enhancing green-excitation efficiency for solar energy utilization: Red phosphors Ba2ZnS3: Eu2+, X–co-doped halide ions (X=Cl, Br, I), Inorg. Chem. 56 (10) (2017) 5720–5727.

[18] C.-W. Lee, V. Petrykin, M. Kakihana, Synthesis and effect of sr substitution on fluorescence of new Ba2- xSrxZnS3: Eu2+ red phosphor: Considerable enhancement of emission intensity, J. Cryst. Growth 311 (3) (2009) 647–650.

[19] M. Rakshit, S. Chowdhury, A. Majumdar, D. Banerjee, D. Jana, A first-principles study of ternary metal chalcogenides Ba2MnX3 (X= Te, Se, S) for efficient thermoelectric applications empowered by machine-learning interatomic potential, Comput. Mater. Sci. 230 (2023) 112526.

[20] P. Blaha, K. Schwarz, G.K. Madsen, D. Kvasnicka, J. Luitz, et al., wien2k, 2001, An augmented plane wave+ local orbitals program for calculating crystal properties, Vol. 60, No. 1.

[21] P. Blaha, K. Schwarz, F. Tran, R. Laskowski, G.K. Madsen, L.D. Marks, WIEN2k: An APW+ lo program for calculating the properties of solids, J. Chem. Phys. 152 (7) (2020).

[22] G. Seifert, Tight-binding density functional theory: an approximate Kohn- Sham DFT scheme, J. Phys. Chem. A 111 (26) (2007) 5609–5613.

[23] J.P. Perdew, K. Burke, M. Ernzerhof, Generalized gradient approximation made simple, Phys. Rev. Lett. 77 (18) (1996) 3865.

[24] A.D. Becke, E.R. Johnson, A simple effective potential for exchange, J. Chem. Phys. 124 (22) (2006).

[25] G.K. Madsen, J. Carrete, M.J. Verstraete, BoltzTraP2, a program for interpolating band structures and calculating semi-classical transport coefficients, Comput. Phys. Comm. 231 (2018) 140–145, http://dx.doi.org/10.1016/j.cpc.2018.05.010.

[26] C.B. Shoemaker, Relationships between structures derived from complex halogenides R2mx3, Z. Kristallographie-Crystall. Mater. 137 (4) (1973) 225–239.

[27] M.R. Harrison, A. Maignan, V. Hardy, O.I. Lebedev, N.A. Young, M.G. Francesconi, Structure and electronic properties of the quasi-one-dimensional Ba2Co1–x Zn x S3 series, Inorg. Chem. 56 (1) (2017) 213–223.

[28] H. Steinfink, I. Grey, Crystal structure of Ba2MnSe3. Linear antiferromagnetism in Ba2MnX3 (X=S, Se), Inorg. Chem. 10 (4) (1971) 691–696.

[29] S. Grimme, S. Ehrlich, L. Goerigk, Effect of the damping function in dispersion corrected density functional theory, J. Computat. Chem. 32 (7) (2011) 1456–1465.

[30] R.T. Shannon, C.T. Prewitt, Effective ionic radii in oxides and fluorides, Acta Crystallogr. B: Struct. Crystallogr. Crystal Chem. 25 (5) (1969) 925–946.

[31] E.K. Mahmoud, A.A. Farghali, S. El-dek, M. Taha, Structural stabilities, mechanical and thermodynamic properties of chalcogenide perovskite ABS3 (A=Li, Na, K, Rb, Cs; B=Si, Ge, Sn) from first-principles study, Eur. Phys. J. Plus 137 (9) (2022) 1006.

[32] W.C. Ermler, R.B. Ross, P.A. Christiansen, Spin-orbit coupling and other relativistic effects in atoms and molecules, in: Advances in Quantum Chemistry, vol. 19, Elsevier, 1988, pp. 139–182.

[33] M. Mohyedin, M. Taib, A. Radzwan, A. Shaari, M. Mustaffa, B. Haq, M. Yahya, First principles study of the effect of spin-orbit coupling on thermoelectric properties of bismuth telluride, Computat. Theoret. Chem. 1182 (2020) 112851.

[34] H. Xiao, J. Tahir-Kheli, W.A. Goddard III, Accurate band gaps for semiconductors from density functional theory, J. Phys. Chem. Lett. 2 (3) (2011) 212–217.

[35] G. Rehman, M. Shafiq, Saifullah, R. Ahmad, S. Jalali-Asadabadi, M. Maqbool, I. Khan, H. Rahnamaye-Aliabad, I. Ahmad, Electronic band structures of the highly desirable III–V semiconductors: TB-mBJ DFT studies, J. Electron. Mater. 45 (2016) 3314–3323.

[36] W. Setyawan, S. Curtarolo, High-throughput electronic band structure calculations: Challenges and tools, Comput. Mater. Sci. 49 (2) (2010) 299–312.

[37] D.R. Santos, S. Shukla, B. Vermang, Prospects of copper–bismuth chalcogenide absorbers for photovoltaics and photoelectrocatalysis, J. Mater. Chem. A (2023).

[38] A. Bouhemadou, O. Boudrifa, N. Guechi, R. Khenata, Y. Al-Douri, Ş. Uğur, B. Ghebouli, S. Bin-Omran, Structural, elastic, electronic, chemical bonding and optical properties of Cu-based oxides ACuO (A=Li, Na, K and Rb): An ab initio study, Comput. Mater. Sci. 81 (2014) 561–574.

[39] J. Bardeen, W. Shockley, Deformation potentials and mobilities in non-polar crystals, Phys. Rev. 80 (1) (1950) 72.

[40] K. Kaasbjerg, K.S. Thygesen, K.W. Jacobsen, Phonon-limited mobility in n-type single-layer MoS 2 from first principles, Phys. Rev. B 85 (11) (2012) 115317.

[41] X. Li, X. Zuo, X. Jiang, D. Li, B. Cui, D. Liu, Enhanced photocatalysis for water splitting in layered tin chalcogenides with high carrier mobility, Phys. Chem. Chem. Phys. 21 (14) (2019) 7559–7566.

[42] C. Sujith, S. Joseph, T. Mathew, V. Mathew, Ab initio investigation of the structural and electronic properties of tantalum thallium chalcogenides TaTlX3 (X=S, Se), J. Solid State Chem. 315 (2022) 123534.

[43] M.S. Yaseen, J. Sun, H. Fang, G. Murtaza, D.S. Sholl, First-principles study of electronic and optical properties of ternary compounds AuBX2 (X=S, Se, Te) and AuMTe2 (M=Al, In, Ga), Solid State Sci. 111 (2021) 106508.

[44] A. Forouhi, I. Bloomer, Optical properties of crystalline semiconductors and dielectrics, Phys. Rev. B 38 (3) (1988) 1865.

[45] C. Ambrosch-Draxl, J.O. Sofo, Linear optical properties of solids within the full-potential linearized augmented planewave method, Comput. Phys. Commun. 175 (1) (2006) 1–14.

[46] V. Chethan, C. Sujith, T. Mathew, M. Mahendra, The quest for optimal photovoltaics: A theoretical exploration of quasi-one-dimensional tin based chalcogenides XSnS3 (X=Ba, Sr), Mater. Today Commun. 37 (2023) 107501.

[47] M. Faizan, S.H. Khan, H. Khachai, T. Seddik, S.B. Omran, R. Khenata, J. Xie, M.m. AL-Anazy, Electronic, optical, and thermoelectric properties of perovskite variants A2bx6: Insight and design via first-principles calculations, Int. J. Energy Res. 45 (3) (2021) 4495–4507.

[48] H. Labrim, A. Jabar, L. Laanab, B. Jaber, L. Bahmad, Y. Selmani, S. Benyoussef, Optoelectronic and thermoelectric properties of the perovskites: NaSnX3 (X=Br or I)—a DFT study, J. Inorganic Organometall. Polymers Mater. 33 (10) (2023) 3049–3059.

[49] D.J. Cirilo-Lombardo, Semiconductor dielectric function, excitons and the penn model, Phil. Mag. 95 (9) (2015) 1007–1015.

[50] S. Al-Qaisi, M. Mushtaq, S. Alomairy, T.V. Vu, H. Rached, B.U. Haq, Q. Mahmood, M. Al-Buriahi, First-principles investigations of Na2CuMCl6 (M=Bi, Sb) double perovskite semiconductors: materials for green technology, Mater. Sci. Semicond. Process. 150 (2022) 106947.

[51] H. Bennacer, S. Berrah, A. Boukortt, M.I. Ziane, Electronic and optical properties of GaInX 2 (X=As, P) from first principles study, NISCAIR-CSIR, India, 2015.

[52] A. Poglitsch, D. Weber, Dynamic disorder in methylammoniumtrihalogenoplumbates (II) observed by millimeter-wave spectroscopy, J. Chem. Phys. 87 (11) (1987) 6373–6378.

[53] M. Sendner, P.K. Nayak, D.A. Egger, S. Beck, C. Müller, B. Epding, W. Kowalsky, L. Kronik, H.J. Snaith, A. Pucci, et al., Optical phonons in methylammonium lead halide perovskites and implications for charge transport, Mater. Horiz. 3 (6) (2016) 613–620.

[54] S. Singh, Refractive index measurement and its applications, Phys. Scr. 65 (2) (2002) 167.
[55] T. Moss, Relations between the refractive index and energy gap of semiconductors, Phys. Status Solidi (B) 131 (2) (1985) 415–427.
[56] D.F. Swinehart, The beer-lambert law, J. Chem. Edu. 39 (7) (1962) 333.
[57] A. Ojha, R.K. Sabat, S. Bathula, Advancement in half-Heusler thermoelectric materials and strategies to enhance the thermoelectric performance, Mater. Sci. Semicond. Process. 171 (2024) 107996.
[58] A.B. Siad, H. Riane, M. Siad, F. Dahou, A. Allouche, M. Baira, Elevating energy device potential: exploring optoelectronic and thermoelectric advantages in stable double perovskites K2NaInX6 (X=F, Cl, Br, I) via Ab initio analysis, J. Mater. Sci. (2024) 1–19.
[59] G.K. Madsen, D.J. Singh, BoltzTraP. a code for calculating band-structure dependent quantities, Comput. Phys. Comm. 175 (1) (2006) 67–71.
[60] M. Bilal, B. Khan, H.R. Aliabad, M. Maqbool, S.J. Asadabadi, I. Ahmad, Thermoelectric properties of SbNCa3 and BiNCa3 for thermoelectric devices and alternative energy applications, Comput. Phys. Comm. 185 (5) (2014) 1394–1398.
[61] Z.U. Abdin, I. Qasim, M. Rashid, A. Mera, B.U. Haq, Q. Mahmood, First principle study of optoelectronic and thermoelectric properties of (Cs/Rb) AuI3 for clean energy, Mater. Sci. Semicond. Process. 147 (2022) 106759.
[62] The first-principle study of mechanical, optoelectronic and thermoelectric properties of CsGeBr3 and CsSnBr3 perovskites.
[63] T. Takeuchi, Conditions of electronic structure to obtain large dimensionless figure of merit for developing practical thermoelectric materials, Mater. Trans. 50 (10) (2009) 2359–2365.
[64] K. Biswas, J. He, I.D. Blum, C.-I. Wu, T.P. Hogan, D.N. Seidman, V.P. Dravid, M.G. Kanatzidis, High-performance bulk thermoelectrics with all-scale hierarchical architectures, Nature 489 (7416) (2012) 414–418.
[65] Y. Chen, H. Yi, X. Wu, R. Haroldson, Y. Gartstein, Y. Rodionov, K. Tikhonov, A. Zakhidov, X.-Y. Zhu, V. Podzorov, Extended carrier lifetimes and diffusion in hybrid perovskites revealed by Hall effect and photoconductivity measurements, Nat. Commun. 7 (1) (2016) 12253.